The Hamburg meteorite fall: Fireball trajectory, orbit, and dynamics

P. G. BROWN [1,2*], D. VIDA[3], D. E. MOSER[4], M. GRANVIK[5,6], W. J. KOSHAK[7], D. CHU[8],
J. STECKLOFF[9,10], A. LICATA[11], S. HARIRI[12], J. MASON[13], M. MAZUR[3], W. COOKE[14], and
Z. KRZEMINSKI[1]

[1]Department of Physics and Astronomy, University of Western Ontario, London, Ontario N6A 3K7, Canada
[2]Centre for Planetary Science and Exploration, University of Western Ontario, London, Ontario N6A 5B7, Canada
[3]Department of Earth Sciences, University of Western Ontario, London, Ontario N6A 3K7, Canada
[4]Jacobs Space Exploration Group, EV44/Meteoroid Environment Office, NASA Marshall Space Flight Center, Huntsville,
Alabama 35812, USA
[5]Department of Physics, University of Helsinki, P.O. Box 64, 00014 Helsinki, Finland
[6]Division of Space Technology, Luleå University of Technology, Box 848, Kiruna S-98128, Sweden
[7]NASA Marshall Space Flight Center, ST11 Robert Cramer Research Hall, 320 Sparkman Drive, Huntsville,
Alabama 35805, USA
[8]Chesapeake Aerospace LLC, Grasonville, Maryland 21638, USA
[9]Planetary Science Institute, Tucson, Arizona 85719, USA
[10]Department of Aerospace Engineering and Engineering Mechanics, University of Texas at Austin, Austin, Texas 78705, USA
[11]Farmington Community Stargazers, Farmington Hills, Michigan 48334, USA
[12]Department of Physics and Astronomy, Eastern Michigan University, Ypsilanti, Michigan 48197, USA
[13]Orchard Ridge Campus, Oakland Community College, Farmington Hills, Michigan 48334, USA
[14]NASA Meteoroid Environment Office, Marshall Space Flight Center, Huntsville, Alabama 35812, USA
*Corresponding author. E-mail: pbrown@uwo.ca

Abstract–The Hamburg (H4) meteorite fell on 17 January 2018 at 01:08 UT approximately 10 km north of Ann Arbor, Michigan. More than two dozen fragments totaling under 1 kg were recovered, primarily from frozen lake surfaces. The fireball initial velocity was 15.83 ± 0.05 km s^{-1}, based on four independent records showing the fireball above 50 km altitude. The radiant had a zenith angle of $66.14 \pm 0.29°$ and an azimuth of $121.56 \pm 1.2°$. The resulting low inclination (<1°) Apollo-type orbit has a large aphelion distance and Tisserand value relative to Jupiter (T_j) of ~3. Two major flares dominate the energy deposition profile, centered at 24.1 and 21.7 km altitude, respectively, under dynamic pressures of 5–7 MPa. The Geostationary Lightning Mapper on the Geostationary Operational Environmental Satellite-16 also detected the two main flares and their relative timing and peak flux agree with the video-derived brightness profile. Our preferred total energy for the Hamburg fireball is 2–7 T TNT ($8.4–28 \times 10^9$ J), which corresponds to a likely initial mass in the range of 60–225 kg or diameter between 0.3 and 0.5 m. Based on the model of Granvik et al. (2018), the meteorite originated in an escape route from the mid to outer asteroid belt. Hamburg is the 14th known H chondrite with an instrumentally derived preatmospheric orbit, half of which have small (<5°) inclinations making connection with (6) Hebe problematic. A definitive parent body consistent with all 14 known H chondrite orbits remains elusive.

INTRODUCTION

Measuring the preimpact orbits for meteorites provides a unique linkage between laboratory-based meteorite studies and asteroid science. Meteorite orbits immediately prior to Earth impact represent the final stage in a long stochastic process of orbital migration of meteorites from the main asteroid belt to Earth

(Vokrouhlický and Farinella 2000). With sufficient numbers of meteorite orbits, statistical inferences as to the origin of particular meteorite group source regions in the Main Belt may be made (Granvik and Brown 2018) which ultimately may provide unique constraints as to the original parent bodies for some groups of meteorites.

As of late 2018, 27 meteorite orbits have been published (Borovička et al. 2015; Devillepoix et al. 2018; Granvik and Brown 2018) with at least seven more having sufficient data for orbit determination but not yet published. Among these are 13 H chondrites with measured orbits, by far the largest of any meteorite group.

The Main Belt source region of the H chondrites remains unclear. Gaffey and Gilbert (1998) proposed the large Main Belt asteroid (6) Hebe to be the primary parent body for the H chondrites, based on its similar reflectance spectra to H chondrites, size and location near the 3:1 (Jovian) mean-motion resonance (MMR) and the ν_6 secular resonance, both major escape routes (ER) from the main asteroid belt. More recently, other Main Belt asteroids with reflectance spectra consistent with H chondrites have also been found (Vernazza et al. 2014) throughout the Main Belt. Fieber-Beyer and Gaffey (2014) found several small, H chondrite-like asteroids proximal to (6) Hebe and suggested a family linkage. Most recently, however, Marsset et al. (2017) used high resolution imagery of (6) Hebe to rule out an impact basin large enough to be consistent with the total volume of these nearby smaller H chondrite-like asteroids. Finally, NEAs found to have compatible H chondrite reflectance spectra also appear to be most likely delivered from the 3:1 MMR, but with some contribution from the 5:2 MMR and ν_6 possible (Binzel et al. 2015). Taken together, current evidence suggests that ERs for the H chondrites ranging in distance from the 3:1 to as far as the 5:2 MMR resonance are all plausible candidates; the role of (6) Hebe in the delivery picture remains unclear.

Here, we describe instrumental records of the fall of the Hamburg (H4) meteorite (Heck and Greer 2018). These data include direct camera recordings of the fireball, brightness measurements of the fireball recorded by the Geostationary Lightning Mapper (GLM) on the GOES-16 satellite, Doppler weather data recording the atmospheric meteorite debris plume, as well as meteorite recovery locations. From these data, we have estimated the preatmospheric orbit and initial mass of the Hamburg meteorite and use this information to estimate the probability that Hamburg is derived from (6) Hebe in addition to its relationship to ERs common to other H chondrites.

GENERAL CIRCUMSTANCES OF THE METEORITE FALL AND OVERVIEW OF INSTRUMENTAL RECORDS

The Hamburg fireball occurred at 01:08:29 UTC (20:08:29 EST) on January 17, 2018 (Jan 16 local time) over Southeastern Michigan, USA. The fireball was widely seen by numerous eyewitnesses, with more than 650 submitting fireball reports to the American Meteor Society (Perlerin 2018) from seven U.S. states and the Canadian province of Ontario. Sonic booms from the fireball were also reported by many eyewitnesses and seismo-acoustic coupling of this shock was detected at a nearby infrasonic and seismic stations (Hedlin et al. 2018) while the infrasonic wave was also detected at the ELFO infrasound array (Silber and Brown 2014) in Ontario. Additionally, Doppler weather radar detected the falling debris plume of meteorites shortly after the fireball. Cloud conditions at the time were unfavorable —most of Southern Ontario and large portions of Michigan and Ohio were nearly overcast making direct visibility of the fireball challenging. Figure 1 shows the cloud conditions in the region at the time of the fireball.

Despite the poor weather, many casual video recordings of the meteor were secured. In total, we geolocated 27 unique videos showing either the direct fireball or its indirect scattered light. The all sky cameras of the Southern Ontario Meteor Network (Brown et al. 2010) and NASA All Sky Fireball Network (Cooke and Moser 2012) were largely overcast at the time, though many stations showed two distinct flashes as the fireball illuminated clouds at ranges in excess of 400 km, providing timing checks on the two major flares. One NASA all sky camera in Oberlin, OH (Fig. 2a), had partial clear sky and recorded much of the fireball through thin, high clouds.

From among these 27 casual video recordings, four were selected which showed a direct view of the fireball and were in fixed positions allowing direct astrometric calibration. In all four cases, we were able to later obtain nighttime stellar calibration data for the same systems. All cameras had generally unchanged pointing since the time of the fireball permitting plate calibrations; small changes in some calibration images were corrected manually. Two additional records were selected for use in relative photometry measurements. These two were selected because one contained a local light source which we used to remove the effects of the cameras' automatic gain control on the photometry from the relative brightness of scattered light on the ground while the other one (the Oberlin all sky video) had an unsaturated direct view of the fireball for the early to middle portion
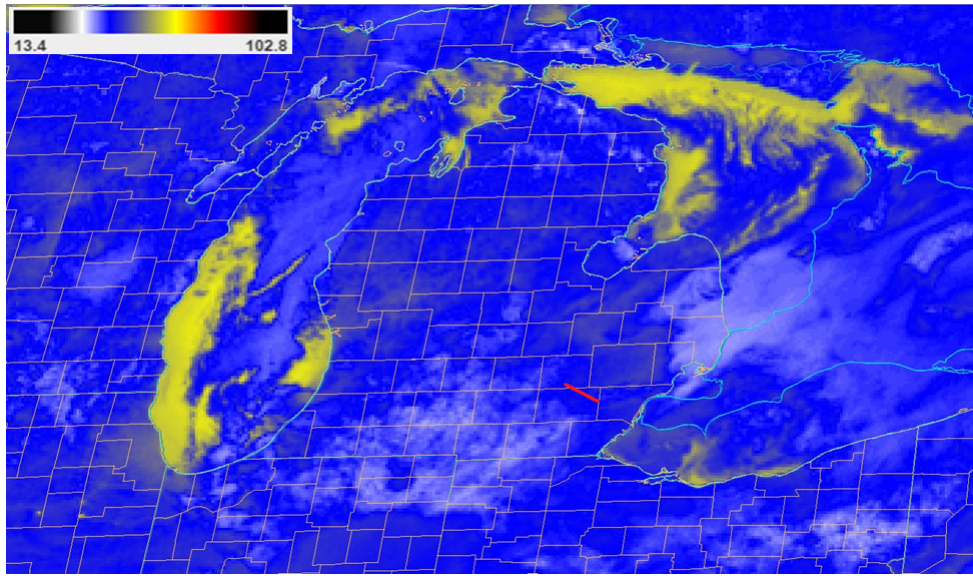
Fig. 1. Regional map overview showing cloud cover as measured by the GOES 16 Advanced Baseline Imager (Level 1b data) at 01:02 UT on January 17, 2018 in the area where the fireball (red line) was visible. These images are in the 10.35 μm band and are showing longwave IR radiance (color bar) in units of $mW/(m^2 \, sr \, cm^{-1})$. Credit: NASA SPoRT/Kevin M. McGrath.

of the trajectory. Table 1 lists the details of these five casual video records and the Oberlin all sky camera data.

The most complete record of the fireball among these calibrated videos were from Defiance, OH, Chicago, IL, Brant, ON and Madison, WI. That the best recordings are from very distant cameras reflects the heavy cloud cover in the vicinity of the fireball trajectory, which greatly reduced visibility of the fireball for all cameras with ranges under 100 km. The Oberlin, OH, NASA all sky camera detected the fireball behind thin, high clouds in the early portion of the trajectory and had a substantially worse pixel scale than the other cameras; it was not used in the final astrometric solution. Figure 2 displays individual frames showing the fireball from early portions of Oberlin, Defiance, Chicago, and Madison where the images are unsaturated. Two bright flares dominate the late stages of flight for all cameras, with the fireball remaining luminous to a height of 19.7 km.

Fireball Trajectory and Orbit

All cameras had positional calibrations using background stars for each of the four fixed cameras, generally taken within a few days to at most a few weeks of the event. In most cases, the cameras remained fixed and no noticeable change in orientation was apparent using nearby objects as a guide. Astrometric plates were computed using two third-order polynomial fits as described in Weryk and Brown (2012). Although the individual frame picks were often uncertain due to

clouds or blooming, the stations had good intersection geometry and small pixel scales. As a result, we found the trajectory orientation to be quite robust (less than a degree of variance) under inclusion of different combinations of stations and points. Figure 3 shows the camera locations relative to the fireball path and meteorite strewn field. The details of the calibration for each of these four sites, including plots of plate residuals, are given in Appendix S1 in supporting information. The supporting information also contains plots and tables related to the final trajectory and orbit as well as all individual astrometric picks for all four stations. Note that for the Madison, WI, site, a radial plate fit (Borovička 2014) was found to produce slightly better agreement with the trajectory as compared to other sites and this was used for the final trajectory solution.

Figure 4 shows the resulting lateral deviations (positive indicating a sightline passed above the final trajectory) from a straight-line fit. We show all four stations where measurements were made. All station weights were equal. The trajectory was computed using a line of sight (LoS) trajectory optimization routine similar to Borovička (1990). As described in Vida et al. (2019), this technique uses a Monte Carlo formalization of the LoS solver, estimating the mathematical fit uncertainty based on the variance of measurements from each station and implementing Earth rotation at all points. This produces a lower bound to the total uncertainty in the trajectory measurement. The best estimate for the orbital and radiant uncertainties is based on the variation in the
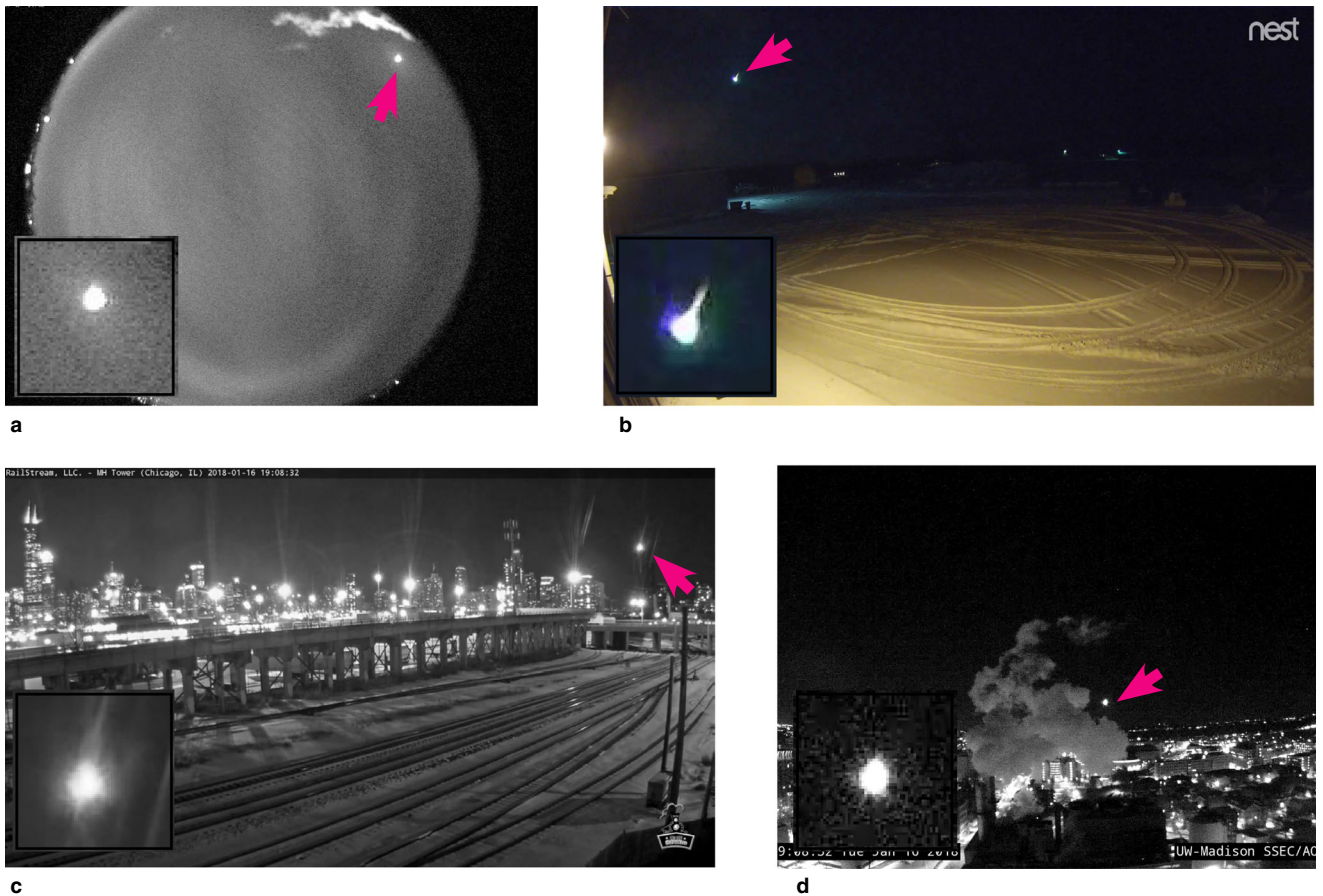
Fig. 2. The Hamburg fireball as seen from Oberlin, OH [16] (a), from Defiance, OH [95] (b), Chicago, IL [97] (c), and from Madison, WI [1] (d). The arrow points to the fireball in each frame with the inset showing a zoomed in region near the tip of each arrow for clarity. Credits: NASA MEO, the Baden Family, Railstream, LLC/Andrea Mercatante and Michael Kisser, and UW–Madison SSEC/AOS, respectively.

trajectory found by iteratively removing outlying points from various stations and noting the maximal change to the radiant and velocity. Finally, an approximate upper bound to the speed uncertainty was found by using the standard deviation of the individual station speed measurements (see Table S3 in Appendix S1 for details). Table 2 summarizes the final trajectory solution.

The estimation of the fireball orbit is critically dependent on the initial velocity; that is, the velocity before measurable deceleration takes place due to atmospheric drag. This height depends on the camera system and its resolution and the geometry and number of cameras relative to the trajectory. It also depends on the meteoroid mass, speed, and entry angle (e.g., Vida et al. 2018). This deceleration height varies from over 100 km altitude for small, slow, shallow-entry meteoroids, to very low heights for larger (decimeter to meter-sized), steeper events. We found that noticeable deceleration did not become apparent in the solutions for the steeply entering Hamburg fireball until below 50 km altitude. This is consistent with our entry modeling (see Discussion), which predicts total deceleration was less than 0.1 km s^{-1} above 50 km height. The four astrometrically calibrated cameras had average ECF speed estimates between 15.6 and 15.9 km s^{-1} based on the trajectory visible from each station above 50 km height, with an average speed of 15.78 ± 0.14 km s^{-1}. The uncertainty here represents the spread in the independent speeds across all four cameras and does not account for any other systematic effects. However, that four independently calibrated cameras all produce similar initial average speeds provides confidence this is a physically reasonable range for the initial speed. The final best estimate of the initial velocity based on simultaneous fitting of the length versus time for all cameras including timing offsets using the method described in Vida et al. (2019) is 15.83 ± 0.05 km s^{-1}. The uncertainty here represents the spread in speeds for different solutions where outlying points are removed, capturing an estimate of

Table 1. Details of videos used in astrometric and photometric measurements of the Hamburg fireball. Station numbering given in the figures is shown in square brackets under the video location where applicable. Videos used for astrometry [A], photometry [P] also indicated after location name.

Video location URL	Latitude, longitude (N/W) (°)	Frame rate (frames per second)	Duration of fireball signal (s)	Field of view (H × V) (°)	Sensor resolution (H × V) (pixels)	Range to endpoint (km)
Ypsilanti, MI[a] [P] [27]	42.2728, 83.5985	15	2	–	1920 × 1080	44
Defiance, OH[b] [A,P] [95]	41.2431, 84.3641	15	4.1	70 × 35	1200 × 600	155
Oberlin, OH (NASA) [P] [16]	41.2928, 82.2225	30	4.4	360 × 90	640 × 480	190
Brant, ON[c] [A] [99]	43.2126, 80.2310	1	4	84 × 51	2688 × 1520	307
Chicago, IL[d] [A] [2]	41.8602, 87.6412	30	4.1	60 × 24	1500 × 600	320
Madison, WI[e] [A,P] [1]	43.0707, 89.4069	7.7	3.4	76 × 47	1280 × 960	453

[a]https://www.youtube.com/watch?reload=9&v=mu0BpkFSPJU
[b]https://twitter.com/BadenElizabeth/status/953745866518560770
[c]https://www.youtube.com/watch?v=jHIu_Kz3srU
[d]https://www.youtube.com/watch?v=2OEw7YkyXKQ
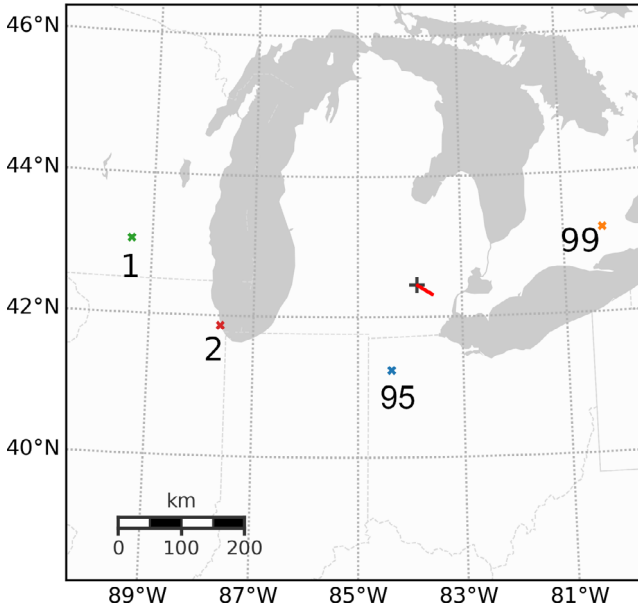[e]https://www.youtube.com/watch?v=8Pf5739vHoU

Fig. 3. Location of cameras used for astrometric measurements and ground track (red line) of the Hamburg fireball. Station numbering corresponds to names given in Table 1.

Fig. 4. Lateral residuals from all stations relative to the final straight−line solution for the Hamburg fireball. Station numbering corresponds to values in Table 1 with 95—Defiance, OH, 99—Brant, ON, Canada, 1—Madison, WI, and 2—Chicago, IL.

the systematic errors present. The resulting orbit, computed following the procedure in Ceplecha (1987), is given in Table 3.

The computed orbit has an aphelion close to Jupiter. The Tisserand value with respect to Jupiter is 2.99 ± 0.003. Such an orbit is borderline between asteroidal and Jupiter-family comet-type orbits and would appear to be odd for an H chondrite. However, of the 13 previously published H chondrite orbits, two
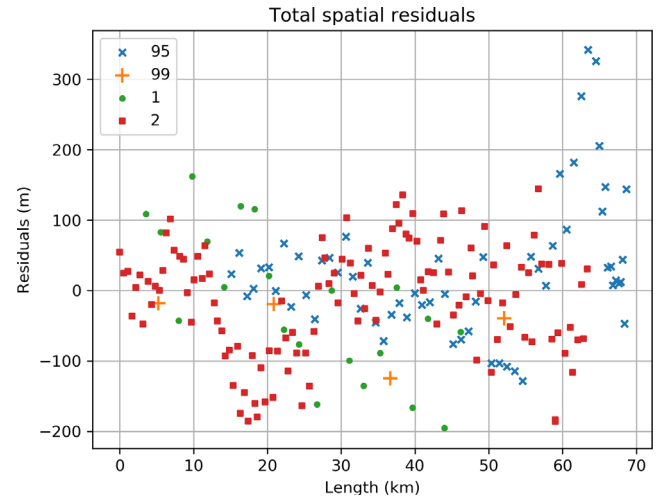
have similarly low T_j of ~3 values (Ejby and Kosice) and two others have $T_j < 3.1$ (Benesov and Murrili; Granvik and Brown 2018).

FIREBALL LIGHTCURVE

Video Data

Reconstruction of the fireball lightcurve from video observations was challenging due to cloud conditions and saturation. Two strong flares near the end of the trajectory were visible on most videos and are localized

Table 2. The atmospheric trajectory for the January 17, 2018 Hamburg fireball based on four calibrated camera measurements. Geographic coordinates are referenced to the WGS84 geoid and all local quantities are in an Earth centred fixed (ECF) frame. Uncertainties represent the best overall estimate of the error in speed and radiant. Also shown are error bounds (in square brackets) that represent the uncertainty in mathematical fit (derived from the Monte Carlo uncertainty as described in the text) as a lower error estimate and the SD of the interstation speed as an upper error estimate.

	Beginning	End
Height (km)	83.02 ± 0.01	19.73 ± 0.01
Latitude (N)	42.320 ± 0.0001	42.451 ± 0.0001
Longitude (W)	83.567 ± 0.0005	83.857 ± 0.0002
Slope	66.14 ± 0.29 [0.02, 0.29]	
Azimuth of radiant	121.56 ± 1.2 [0.13, 1.2]	
Velocity (km s^{-1})	15.83 ± 0.05 [0.01, 0.14]	<6
Trail length/ duration	68.7 km/>4.2 s	
Time (UT)	01 h08 m29 s	01 h08 m34 s

in time to within one video frame in all videos. We were able to use the timing of these two flares to compute the relative timing between each video. Our reconstruction of the fireball lightcurve from direct and indirect (scattered) intensity is shown in Fig. 5. Our approach was to use the relative change in brightness (either direct or scattered from surfaces in the video) from the most reliable video segments and assume that all offsets between the videos are multiplicative so that the slopes are matched. This is broadly similar to the approach used for the Chelyabinsk (Brown et al. 2013), Kosice (Borovička et al. 2013a), and Jesenice (Spurný et al. 2010) meteorite-producing fireballs.

The earliest portion of the fireball was directly visible from Madison, WI. Several stars visible in the same frames at almost the same altitude as the fireball were used to calibrate the absolute brightness of the rising portion of the fireball using standard meteor aperture photometry techniques (e.g., Weryk and Brown 2012) from this distant station for the first second of visibility of the fireball. After this stage, the fireball saturates the video and is also very low from the Madison station. The unsaturated portions of the direct fireball image from Oberlin and Defiance are used from $t = 1$ s to $t = 2.5$ s after which time all stations become saturated. From $t = 2.5$ s to $t = 4.2$ s, indirect scattering from two regions of snow-covered roof surfaces as visible from the nearby Ypsilanti, Michigan, video was used following the approach of Brown et al. (2013) for Chelyabinsk exploiting a directly visible light source to calibrate changes in the automatic gain control for the

Table 3. Heliocentric orbit for the fireball producing the Hamburg meteorite. All angular coordinates are referenced to J2000.0, except the apparent radiant which is epoch of date and in an Earth centred fixed (ECF) frame. V_∞ refers to the speed of the fireball relative to the Earth's surface prior to significant atmospheric deceleration, which for Hamburg occurs at a height of 50 km. Uncertainties represent the best overall estimate of the error in speed and radiant. Also shown are error bounds (in square brackets) that represent the uncertainty in mathematical fit (derived from the Monte Carlo uncertainty as described in the text) as a lower error estimate and the standard deviation of the interstation speed as an upper error estimate.

α_r	$72.83 \pm 0.34°$ [0.04, 0.34]
δ_r	$27.37 \pm 0.30°$ [0.03, 0.30]
V_∞	15.83 ± 0.05 km s^{-1} [0.01, 0.14]
V_G	11.1 ± 0.07 km s^{-1} [0.01, 0.2]
α_G	$74.29 \pm 0.39°$ [0.05, 0.4]
δ_G	$24.71 \pm 0.36°$ [0.03, 0.36]
a	2.73 ± 0.05 [0.01, 0.11] A.U.
e	0.661 ± 0.006 [0.001, 0.014]
i	$0.604 \pm 0.11°$ [0.01, 0.11]
ω	$211.65 \pm 0.3°$ [0.03, 0.3]
Ω	$296.421 \pm 0.03°$ [0.003, 0.04]
q	0.926 ± 0.001 [0.002, 0.001] A.U.
Q	4.5 ± 0.1 A.U. [0.005, 0.2]
T_j	2.99 ± 0.003 [0.002, 0.01]

camera (see Fig. 6). The latter portion of the fireball from Defiance was also unsaturated and scaled to match the Ypsilanti second flare to produce the end portion of the lightcurve to $t = 4.5$ s. Note that the timing after the second flare is uncertain due to changes in the frame rate of the Defiance camera (as described in Appendix S1). The value shown here is a lower limit.

Matching the lightcurve peaks to the spatial trajectory solution, we find that the first flare occurred at a height of 24.1 km at a time of 01 h 08 m 33.44 s UT and the second at a height of 21.7 km at 01 h 08 m 33.64 s UT. Hedlin et al. (2018) estimated a best-fit flare height between 22 and 24 km based on hypocenter solutions from acoustic arrivals detected at nearby seismic/infrasound stations, agreeing with our result.

OPTICAL ENERGY ESTIMATE FROM THE GLM

The Geostationary Operational Environmental Satellite-16 (GOES-16) weather satellite has onboard the world's first GLM (Goodman et al. 2013), which continuously monitors total lightning (i.e., cloud-to-ground flashes and cloud flashes) across a large region of the Western hemisphere. The GOES-16 GLM has been under calibration/validation evaluation for over a year during its post launch product test (PLPT) phase
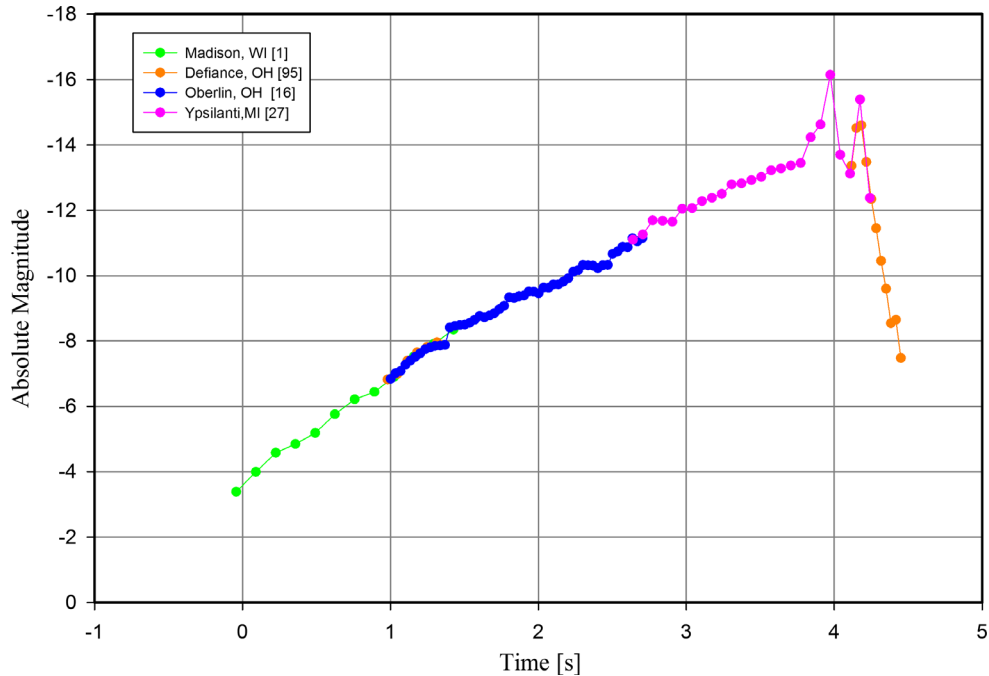
Fig. 5. Lightcurve of the Hamburg fireball based on video records. Time t = 0 corresponds to January 17, 01:08:29.49 UT.

and has reached the "provisional validation level" at the time of this writing. The PLPT evaluation ensures that optimal products are available for both the operational forecasting and broader scientific research communities.

Interestingly, the GLM detected the Hamburg bolide, and therefore provides a unique way to investigate its optical energy characteristics and compare with the video lightcurve. This is not the first bolide to be detected and studied using GLM data; see for example the bolides investigated by Jenniskens et al. (2018).

As described in Goodman et al. (2013), GLM is a high-speed nadir-staring event detector that operates in the near infrared. The narrow band (1 nm) interference filter is centered near a prominent oxygen emission triplet in the lightning spectrum at 777.4 nm. This is the same band employed in the earlier low-Earth-orbit Lightning Imaging Sensor (LIS; Christian et al. 1999) aboard the Tropical Rainfall Measuring Mission satellite. As with LIS, the lens/filter system focuses the input optical radiation onto a high-speed charge-coupled device (CCD) focal plane, and signals are read out in parallel into real-time event processors for pixel-level *event* detection and data compression. The GLM employs a 1372 × 1300 pixel CCD focal plane array with a pixel footprint resolution of about 8 km (at nadir) to about 14 km (at the edge of the field of view). The frame time of the GLM is ~2 ms. Similar to LIS, several techniques are used for detecting lightning both

at day and night. Daytime detection is more challenging because the solar lit thundercloud tops are typically far brighter than the diffuse multiple-scattered cloud-top lightning optical emissions.

Adjacent (side to side, diagonal) pixel-level optical events in one GLM frame define an optical *group*, and optical groups are combined with specific distance/time constraints to define a lightning *flash*; see Mach et al. (2007) for more details, including information on how the fundamental optical event data are clustered and filtered to create the Level 2 GLM group and flash data products. The GLM flash detection efficiency (probability of detection) instrument requirement, presently being validated in the PLPT phase, is 70% with a 5% false (i.e., nonlightning) alarm rate. These values are average criteria over the field of view and over a 24 h period. The GLM location accuracy at the subsatellite point and timing accuracy, also both being validated in the PLPT phase, are to be within 5 km and 1 ms, respectively.

Figure 7 provides a plot of the GLM-detected optical groups produced by the Hamburg bolide. The "stair-step" appearance is an artifact of the ground segment processing algorithm for generating the product distribution and access operational data feed during the GLM provisional validation level period. The instrument optical energy granularity is in reality about a factor of 100 better than the ~1.5 fJ granularity shown in Fig. 7. Nonetheless, the 1.5 fJ granularity is

Fig. 6. Screen capture of two frames of Ypsilanti, Michigan, video showing regions used for relative brightness (square regions—bottom) changes and calibration light sources (circled —top). Image credit Daniel McGhee.

Fig. 7. GLM group energy waveform (black dots) in units of 10^{-15} J and equivalent spectral energy density (red dots) in units of μJm^{-2} $ster^{-1}$ nm^{-1}. Note the drop in the SED from 4.14s to 4.18s is due to the optical groups having two events each, leading to a doubling in the equivalent solid angle of the fireball and an equivalent reduction in the SED.

adequate for the energy estimates for the Hamburg fireball. Note that there is no signal during the "dead interval" from about 4.03–4.14 s in the plot when the fireball emission fell below the detection threshold of the instrument.

All of the optical groups in the bolide were single event groups, except during a period from about 4.14 to 4.18 s when all the groups had two events each. This is when the bolid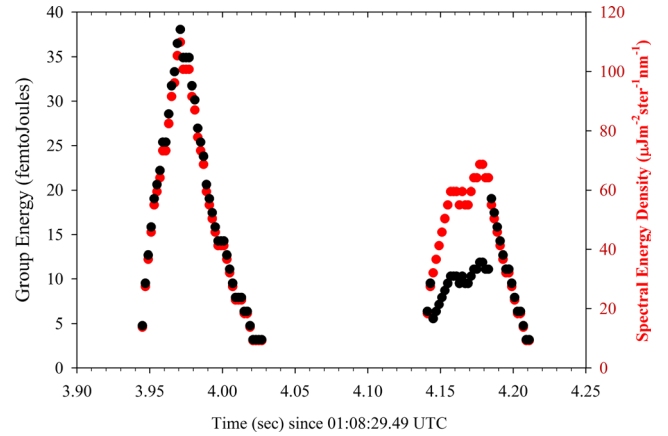e emission crossed a pixel boundary thereby triggering the two adjacent pixels. In turn, this splits the total group energy between the pixels, and also about doubles the total solid angle of the bolide source emission.

Taking into account the GLM entrance pupil area, the pixel solid angle, and the filter bandwidth, the group energy plot can be converted into a spectral energy density (SED) plot as shown in Fig. 7 (red plot). The SED is simply a frame-time integrated radiance in units of μJ m^{-2} sr^{-1} nm^{-1}.

Converting the SED into an equivalent absolute magnitude to compare to the video lightcurve is problematic, given the narrow bandwidth of the GLM detector. This issue is discussed and analyzed extensively in Jenniskens et al. (2018). Under the assumptions adopted in the Jenniskens et al. (2018) analysis of GLM bolide data and accepting their result that the limiting sensitivity for GLM is near peak visual absolute magnitude of −14, we can use the SED and (assuming the floor near an SED of 15 μJ m^{-2} sr^{-1} nm^{-1} is this background) to convert to absolute magnitude and compare to the video lightcurve. The resulting comparison near the peak is shown in Fig. 8. The agreement in relative timing and amplitude for the two flares between the video and GLM lightcurves is very good, providing some confidence in the overall shape and peak values found with the video data alone.

METEORITE DARKFLIGHT MODELING AND COMPARISON TO FALL ELLIPSE

The Hamburg meteorite strewn field lay across a chain of lakes in southern Livingston County, Michigan.
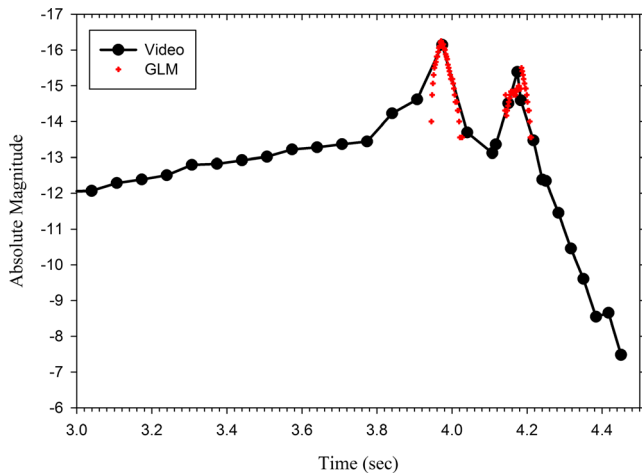
Fig. 8. GLM equivalent spectral energy density (red dots) scaled to absolute astronomical magnitude assuming a noise floor at 15 $Wm^{-2}ster^{-1}nm^{-1}$ is equivalent to $M_v = -14$ compared to the video−derived lightcurve (black dots and line).

These lakes formed at the margin of the Saginaw and Huron lobes of the Laurentide Ice Sheet toward the end of the Wisconsin glaciation (~14 kya). The land between these lakes is heavily populated and largely privately owned. In addition, there is a considerable area of marshes and wetlands in the strewn field, making discovery/recovery of meteorites difficult. Thus, nearly all recovered meteorites were found on top of the lakes. At the time of the fall, these lakes had a thick ice cover (>10 cm) coated with a fresh snowfall. For the 3 days following the fall, no further snow fell, and air temperatures remained below freezing. Meteorites that landed on the lakes were presented as black rocks against a flat, white background. Our group searched Bass Lake, Strawberry Lake, and Hamburg Lake for meteorites. We recovered six samples: three from Strawberry Lake, two on Hamburg Lake, and one on Bass Lake. The Bass Lake find consisted of many small fragments totaling less than a gram, all within a ~2 m radius.

Four days after the fall, the air temperature warmed sufficiently to melt the ice surface, complicating further searches of the lakes. We obtained permission from Hamburg Township to search Manley Bennett Park for meteorites, which shifted our search to land, where we recovered a small meteorite. Additionally, we constructed magnetic sweepers to collect fine magnetic materials from the land surface. These collected materials were heavily contaminated with hematite and magnetite delivered by the Laurentide Ice Sheet. We manually identified and sorted these grains under a microscope, which ultimately revealed two clusterings of meteoritic fragments on the land surface, adding an additional two samples to our total.

To further complete our mapping of the strewn field, we searched local news reports and social media reports for people that found meteorites. We contacted these people to compile the mass and location of their meteorites. We ensured that these reported meteorites had been confirmed as meteoritic by a trained geologist or meteorite hunter, and only include these verified meteorites in our compiled list. Not all contacted persons responded to our enquiry. Nevertheless, this added an additional four new, unreported samples to the total (see Table 4 for masses and locations of all recovered meteorites). Finally, we include in our study the locations of recovered meteorites reported in Heck and Greer (2018).

Figure 9 shows the location of recovered meteorites in the fall area near Hamburg, Michigan, together with the ground projection of the fireball path.

Figure 10 shows the upper winds extracted from radiosonde data from White Lake, Michigan (less than 50 km range from the fireball endpoint), at 0 and 12 UT, the closest radiosonde measurements to the time of the fall at 01:08 UT. Note the large change in wind speed and directions between 5 and 10 km altitude between these times; we do not know how quickly this change occurred. We found linearly interpolating the winds to 1 UT produced darkflight results with a fall line parallel to the fireball trajectory but significantly (~1 km or more) north of Bass and Strawberry Lake, where most finds were located. In contrast, we found that interpolating the winds to 3 AM produced darkflight locations crossing Strawberry and Bass Lakes. As we do not know when the wind shifted, this better agreement between darkflight model results and finds using a 3 AM interpolation is adopted as the more likely wind field, in the absence of finer temporal resolution wind measurements.

To further check that our chosen fireball terminal point is consistent with recovered fragments and attempt to estimate release altitudes for recovered fragments, we use the darkflight model of Ceplecha (1987), which accounts for atmospheric drag, winds, and Earth's rotation. This is used together with the modifications discussed in Brown et al. (2011), who integrate a Monte Carlo approach allowing for a distribution of fragment shapes and velocity perturbations due to fragmentation to estimate the spread in landing locations. In these model runs, individual spherical fragments with masses from 1 kg to 1 g, bracketing the mass range of recoveries [100 g, 0.2 g], are released at the endpoint (19.7 km) and at the height of the two flares (24.1 and 21.7 km). In all simulations, fragments are assumed to have velocities of 3 km s^{-1} at the point of release, consistent with other fireball observations indicating that this is the velocity at which luminous flight ceases (Ceplecha et al. 1998) and are assumed to have a bulk density of 3400 kg m^{-3}

Table 4. Documented Hamburg meteorite recoveries. Locations and mass were directly verified for all specimens; AMS indicates information published by the American Meteor Society at https://www.amsmeteors.org/members/ imo_view/meteorites/2018/168 (accessed August 20, 2018).

Date	Finder	Location	Mass (g)	Notes
January 18, 2018	T. Slisher	42.4485996, −83.8358445	12	Found on lake
January 18, 2018	T. Licata	42.4488509, −83.8385039	15.83	Found on lake
January 18, 2018	B. Wolfe	42.4490422, −83.8483335	26	Found on lake
January 20, 2018	A. Licata	42.4502360, −83.8589170	0.9	Multiple specimens
January 20, 2018	B. Barnibo	42.4362000, −83.7983910	3	Found on lake
January 20, 2018	E. Licata	42.4351030, −83.7943220	0.301	Found on lake
January 27, 2018	T. Licata	42.4508390, −83.8226400	10.43	Found in wooded area
January 18, 2018	D. Landry	42.4541500, −83.8641120	20	AMS
January 19, 2018	G. Barger	42.4533040, −83.8608600	11	AMS
January 19, 2018	L. Janes	42.4512560, −83.8603470	20	AMS
January 26, 2018	R. Matthews	42.4507690, −83.8589820	2	AMS
January 26, 2018	L. Matthews	42.4506450, −83.8588070	1	AMS
January 18, 2018	A. Larry	42.4484540, −83.8590680	17.5	AMS
January 18, 2018	Resident	42.4500280, −83.8542220	~60	Witnessed by Brandon Weller, found on land
January 18, 2018	B. Weller	42.4520280, −83.8504440	59.4	AMS
January 18, 2018	R. Ward	42.4511390, −83.8476390	102.6	Largest found fragment—Witnessed by Brandon Weller
January 18, 2018	L. Atkins	42.4488730, −83.8386330	37	AMS
January 20, 2018	L. DeLanoy	42.4471920, −83.8276960	6.5	AMS
January 19, 2018	T.V.	42.4475530, −83.8359690	13.8	
January 19, 2018	T.V.	42.4475140, −83.836789	12.6	
January 19, 2018	T.V.	42.4470070, −83.8384670	11.5	
January 22, 2018	D. Grischke	42.4535890, −83.8560520	55.92	AMS
January 27, 2018	T. Licata	42.4478106, −83.8135184	0.2	Found on air field
January 28, 2018	T. Licata	42.4511370, −83.8532140	0.008	Found in baseball field
January 20, 2018	A. Moritz	42.4573020, −83.8473590	50	
January 18, 2018	Unidentified	42.4512560, −83.8560530	20.6	

appropriate to the average for H chondrites. Note that if the speed at release is higher, ablation will tend to reduce the size of the fragment, but since the trajectory is very steep, the fall point moves only slightly to the west. The nominal prediction for the Hamburg strewn field from these simulations independent of release height produces a fall zone oriented roughly parallel to the direction of the trajectory, but offset slightly to the east and north due to the prevailing winds.

The darkflight line produced by this mass range of fragments falls directly across Bass Lake and Strawberry Lake where most meteorite recoveries were reported as shown in Fig. 11, consistent with our combination of terminal fireball location and wind field. Note that changing the shape factor from that of a sphere to that of a brick (following Halliday et al. 1984) moves fragments to the east while smaller drag coefficient would move fragments to the west along this line. Given the location and masses of recoveries (Fig. 9) in comparison to predictions by release altitude from the fireball, most recovered fragments are consistent with having originated from near the terminal portion of the fireball path, with some locations showing intermixing of various masses.

This could indicate that some of the fragments may have undergone further fragmentation during darkflight. The finds of tens of gram-sized fragments on Bass Lake are several kilometers west of our prediction from the endpoint release. This could also indicate that our trajectory is shifted several hundred meters to the west, that these fragments reached subluminous flight farther west than our measured endpoint, or that the fragments have more streamlined shapes (and hence experience lower drag) than our assumptions. It is also possible that the windfield differs from our adopted model or that the ground scatter is produced by lift forces in flight during the process of fragmentation which have shifted the location of these fragments from a purely drag solution.

To estimate the expected ground scatter of individual fragments released at a given height, we introduce random cross-trajectory speeds consistent with the observations reported by Borovička and Kalenda (2003) for the Morávka fireball. They measured velocities perpendicular to the main fireball trajectory averaging ~50 m s^{-1} (but extending up to 300 m s^{-1}) for individual fragments. We have used the same three release heights as shown in Fig. 11, but add
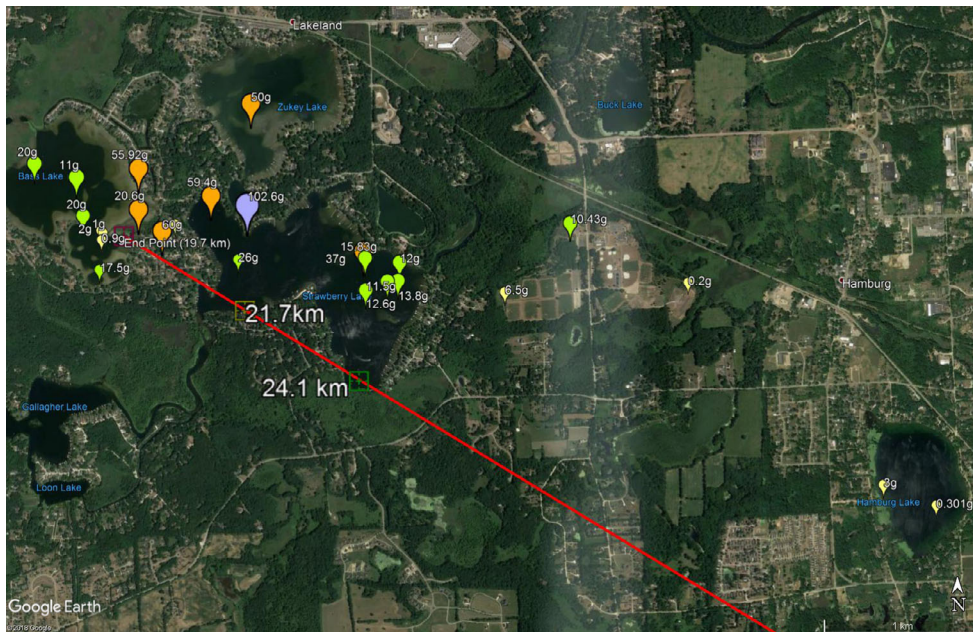
Fig. 9. Recovery locations of meteorites (with measured masses) relative to fireball trajectory (red). Also shown are the location of the first flare at 24.1 km altitude (green square), the second flare at 21.7 km altitude (yellow square), and the endpoint at 19.7 km (purple square).

to each fragment's velocity vector a randomly oriented velocity perturbation of up to 50 m s^{-1}. Our overall procedure follows a similar methodology previously applied to the Grimsby fireball (Brown et al. 2011). Figure 12 shows the resulting spread in fragment fall locations only for terminal altitude of release. The spreads are very similar at the height of the two flares, but are omitted from this figure for clarity. The expected spreads for 10 and 100 g masses may partially explain the large mass intermixing on the lakes, though the westerly finds on Bass Lake remain puzzling. In particular, the recovery of 1–2 g fragments is very difficult to reconcile with the darkflight model from any release altitude; these we interpret as likely late released fragments from larger (tens of gram pieces) which fragmented during darkflight just prior to ground contact, an effect noticed in other large strewn fields (e.g., Bruderheim as discussed in Folinsbee and Bayrock 1961).

The meteorite debris "curtain" was directly observed falling to the ground by the Doppler weather radar station KDTX in Detroit, Michigan, located only 40 km ground range from the fall ellipse. Meteorite debris plumes have been regularly observed by the US NEXRAD Doppler radar systems (Fries and Fries 2010), with more than a dozen meteorite falls in the United States. and Canada having probable NEXRAD signatures (Fries 2018). The NEXRAD systems consist of WSR-88D Doppler weather radars operating at a wavelength of 10 cm with peak power of 750 kW and a beam width of approximately 1° to the 3 dB points (Crum and Alberty 1993).

Spatial comparisons are usually made between darkflight model predictions of fall locations and meteorite recoveries, but with Doppler radar signatures, both spatial and temporal constraints can be introduced to refine release heights of fragments. Such a matching procedure has previously been performed for the Grimsby meteorite fall (Brown et al. 2011).

Figure 13 shows five KDTX sweeps in temporal order starting at 01:12:35 UT and ending at 01:19:58 UT over the fall area. These are the first sweeps which show any reflectivity signal in the area. An earlier sweep covering 1 km altitude occurring ~200 s after the fireball shows no detectable signal. A signal detection during this earlier sweep would correspond to multi-hundreds of grams to kilo-sized fragments released in the final 10 km height interval of the fireball luminous trajectory. This nondetection suggests few such sized fragments were present.

To associate these radar returns with probable release altitudes, we examined a range of fragment masses released at each of the flare heights and the end height to find the best match in time and space with the recorded Doppler signature. Figure 13 shows our best matches color coded to the release points. In general, we are able to match the timing to within a few tens of seconds of the radar returns beginning to the north and
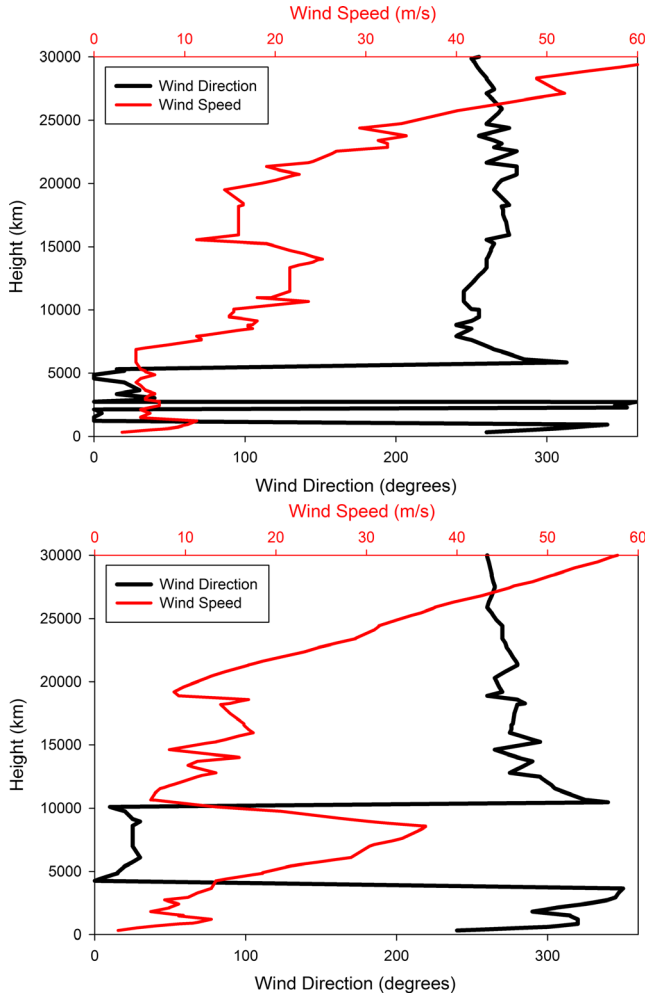
Fig. 10. Upper winds measured by radiosonde released at White Lake, Michigan (https://www.ncdc.noaa.gov/data-access/weather-balloon-data). The top left plot shows the wind field at 0 UT on January 17 while the bottom is the wind field at 12 UT, January 17.

west with masses of tens of grams to 100 g from fragments released at the endpoint. As time progresses, smaller fragments from the endpoint/final flares are reasonable matches in time to the radar returns, though the model fall locations move progressively farther north than the Doppler returns. This difference is comparable to our predicted dispersion based on 50 m s^{-1} SD lateral velocity spreads (see Fig. 12). While the overall match is quite good, there is a northerly skew. This may reflect fragment shapes which are not spherical (and which are therefore blown more southward by the wind) or could be due to the real ground path being several hundred meters farther south than our estimate or variability in the winds.

In summary, the darkflight model and observations are consistent with a scenario whereby 100 g to tens of

gram masses land farthest north/west and arrive first (and are detected in the initial Doppler radar sweeps) with smaller fragments landing progressively later to the east. All of these originate from the very end portion of the trail; release heights of 27–30 km are entirely incompatible with either recovered fall locations or radar sweep timing of any of the fragments. The mixing of recovered fragments with more than an order of magnitude difference in mass in the same locations is an expected feature of such a steep trajectory and has been noted with other steep entries, such as Kosice (Tóth et al. 2015). Small differences in the drag or lift coefficient, late fragmentation during darkflight together with lateral fragmentation forces may cause such mixing.

DISCUSSION

Ablation Entry Model and Initial Mass/Energy

We attempt to estimate the initial mass and approximate fragmentation behavior of the Hamburg fireball by modeling its dynamics and lightcurve and comparing to observations. We focus on a very global match to the overall energetics rather than trying to reconstruct highly detailed fragmentation history as has been done for other meteorite-producing fireballs (e.g., Kosice; Borovička et al. 2013a, 2013b) as we have only coarse dynamic data from videos. In particular, we assume for simplicity that fragmentation points produce light dominated by small particles and not from large fragments.

Specifically, using the estimated initial speed as discussed earlier, we employ the FM model of Ceplecha and ReVelle (2005) to match the lightcurve from Fig. 5 starting at the maximum observed height of the fireball (83 km). This is equivalent to trying to reproduce the energy deposition profile; without detailed matching of the dynamics, this is not a unique solution, but should provide reasonable estimates for the total mass.

The FM model is a numerical implementation of the standard differential single-body equations of meteor flight (Ceplecha et al. 1998), taking into account explicit fragmentation at discrete points into either dust or ponderable fragments. It permits changes in the leading fragment shape-density coefficient, $K = \Gamma A \rho_m^{-2/3}$ where Γ is the drag coefficient, A is the shape factor, and ρ_m is the bulk density of the meteoroid. It also allows for a variable luminous efficiency (τ, where the fireball brightness in absolute magnitude units is given by $M = -0.4 \, (\log \, (\tau dE_k/dt) \, -3.17)$ and E_k is the instantaneous meteoroid kinetic energy in MKS units assuming a 0 magnitude meteor emits 1500 W. We use a fixed intrinsic ablation coefficient of 0.004 s^{-2} km^{-2}
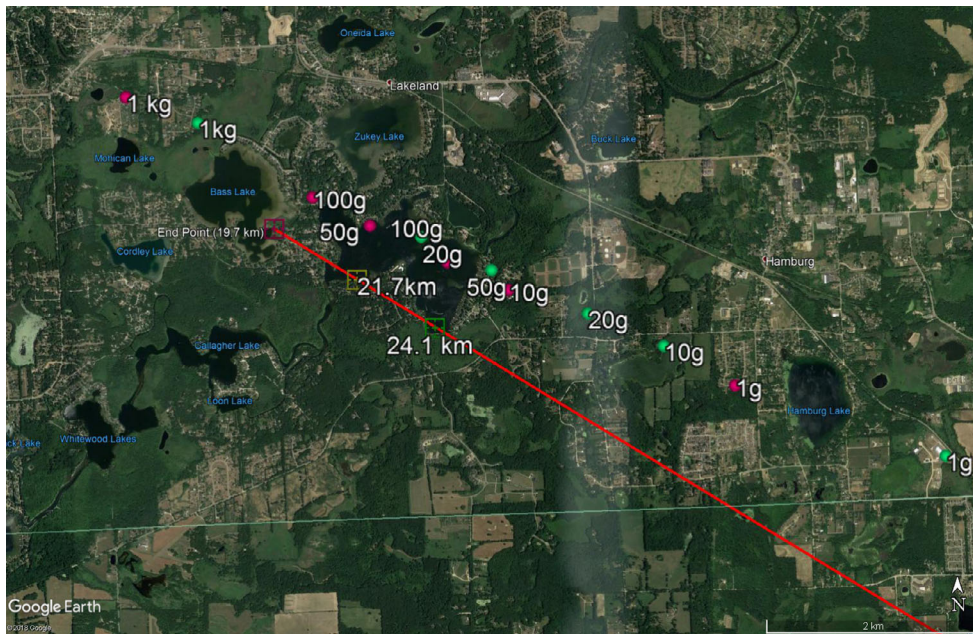
Fig. 11. Darkflight model predicted meteorite fall locations. Predicted fall points at the ground for masses of 1 kg, 100 g, 50 g, 20 g, 10 g, and 1 g are shown released from the endpoint and at the height of the first flare, with the symbols color coded to match the endpoint or first flare.
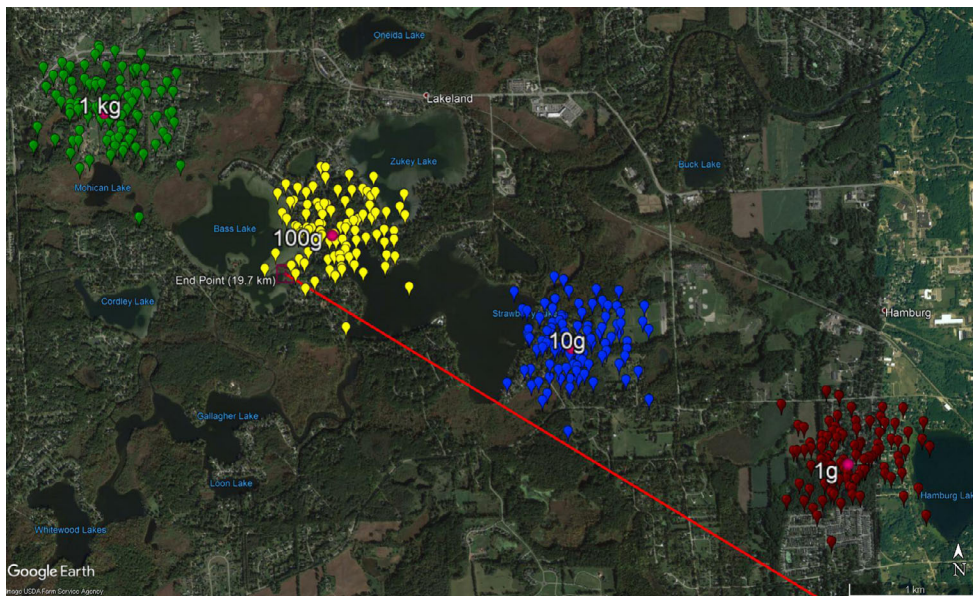

Fig. 12. Dispersion in darkflight fall locations for Monte Carlo spreads of 50 m s^{-1} for fragments released from the fireball endpoint for masses of 1 kg, 100 g, 10 g, and 1 g, respectively (from west to east).

and fixed shape-density coefficient (K) of 0.0046 (MKS) following the approach of Ceplecha and ReVelle (2005) and Borovička et al. (2013a). We do this to restrict the number of free parameters, recognizing that our data with few constraints would not produce meaningful fits if varying these factors. The methodology has been validated through matches with the observed flight characteristics of many well-recorded fireballs, several of
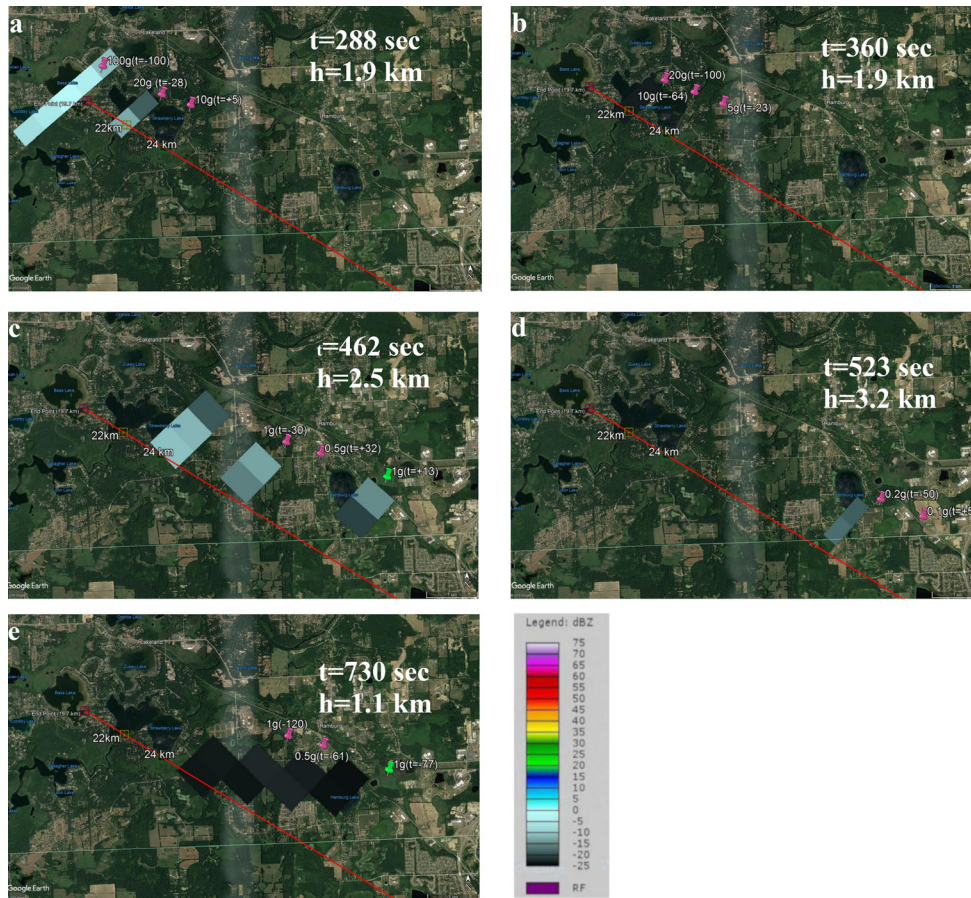
Fig. 13. Doppler radar reflectivity returns from after the Hamburg fireball (panels [a] through [e] respectively—information on time and height are shown in each panel). Note the progression of returns to the East in time reflecting the mass sorting where smaller masses take longer to fall and are blown progressively farther east by the prevailing winds. The sweep height in km is shown for the center of each plot as is the radar signal return strength colorscale (lower right). Shown are the individual best-fit darkflight model matches in location and time for various masses released at different heights. Masses released at the endpoint are shaded purple; those from the first flare are green. The mass and modeled time the fragment fell through the radar beam in seconds either before the beam sweep (negative) or after (positive) are also shown.

which have produced meteorites (Ceplecha and ReVelle 2005).

We use the original luminous efficiency adopted in Ceplecha and ReVelle (2005), which corresponds to values from 0.3% to 1.5% over the full trajectory for Hamburg. Note that Borovička et al. (2013a) have argued that the luminous efficiency relation proposed in Revelle and Ceplecha (2001) is a better match to several recent meteorite-producing fireballs. Those values for the luminous efficiency are three to four times larger than the luminous efficiency used in Ceplecha and ReVelle (2005). Hence, our estimated mass from fitting the lightcurve alone may be considered an upper limit, with masses as low as ~60 kg possible based purely on the lightcurve fit for the highest luminous efficiency values (~5%) proposed by Borovička et al. (2013a).

As much of the videos showing the mid trajectory are saturated, we have no precise dynamic data over this interval and restrict our initial model constraint to matching the lightcurve. Figure 14 shows our best-fit model lightcurve match to the observations. Here, the match was done entirely by trial and error and is representative and not necessarily unique. The estimated total mass for this fit corresponds to 225 kg and the end mass to just over 1 kg. The fits are both reasonable matches to observation.

The model was able to fit the lightcurve assuming no fragmentation until 68 km height at which point a small amount of the total mass (<1%) is released as fine grains to match a small increase in the slope of the lightcurve at this height. This earliest possible fragmentation/disintegration point corresponds to a ram pressure of 27 kPa and is a similarly low value found to

several other meteorite-producing fireballs (e.g., Kosice at 90 kPa; Borovička et al. 2013a). A second slightly more significant jump in the lightcurve near 48 km corresponds to ~1% mass loss as minor fragments/dust under a ram pressure of 0.3 MPa. However, both of these early features are marginal. While their inclusion improves the model fit to the observed lightcurve, these features are also near the limit of our expected uncertainty in early lightcurve reconstruction.

However, the first major flare centred at 24.1 km altitude is well defined and begins at 26.5 km under a dynamic pressure of just over 5 MPa while the second centred at 21.7 km begins at 22.6 km with over 7 MPa of dynamic pressure. These are the most energetic fragmentation events and reflect comparatively high dynamic pressures, similar to the main flare for the Benesov fireball (Borovička and Spurný 1996). The model for the first flare corresponds to a loss of almost 50% of the total remaining mass at this height being consumed to produce dust/small fragments, while the second starting at 22.6 km represents a loss of >90% of the remaining mass at this height to small fragments. This leaves only ~1 kg in the main fragment after the last flare. This does suggest that one or more kilo-sized fragments may have survived after the flares and would have experienced peak dynamic pressures of ~7 MPa, similar to the compressive strengths of the largest fragments which survived other meteorite-producing fireballs (Popova et al. 2011) such as Moravka (Borovička and Kalenda 2003) and Kosice (Borovička et al. 2013a). The dynamic pressure at the flares is also similar to the dynamic pressure at the point of catastrophic disruption for Chelyabinsk, which occurred between 1 and 5 MPa (Borovička et al. 2013b).

The major flares suggest that most of the initial mass survived to under 30 km altitude before being consumed in the two rapid fragmentation events which likely produced most of the recovered fragments. These continued to ablate briefly before reaching subluminous speeds just below the flare altitudes, broadly consistent with the darkflight models.

The main conclusion from this model comparison is that we are able to explain the lightcurve by having the vast majority of the mass of the Hamburg meteoroid ablate to small particles (or dust), with the meteorites reaching the ground as ponderable fragments representing a small fraction (of order only a few percent) of the initial mass.

Our model mass estimate corresponds to a total energy for the Hamburg fireball of ~7 T TNT (or 2.8×10^{10} J) explosive equivalent. This can be compared to the work of Hedlin et al. (2018), who used acoustic periods measured at infrasonic stations near the fireball to estimate yield, a technique commonly
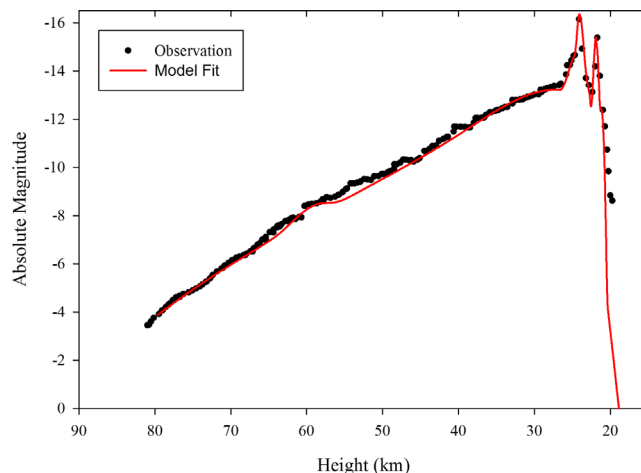

Fig. 14. FM model fit (red line) to observed Hamburg fireball lightcurve (black dots) as a function of height.

applied to bolides (Ens et al. 2012). They estimated a nominal yield for Hamburg to be ~2 T TNT equivalent, with uncertainty bounds ranging from 1 to 8 t TNT. Our estimate overlaps at the high end with that of Hedlin et al. (2018). We note that systematic uncertainties likely influence both results. For example, our model result uses comparatively low luminous efficiencies; adopting those used by other investigators (e.g., Borovička et al. 2013a) would tend to reduce our mass and hence energy estimate by as much as a factor of 3. Similarly, the period estimate from Hedlin et al. (2018) is likely associated with one of the terminal flares (as they note), which would necessarily represent a smaller total energy than the initial event energy. Given these uncertainties, we consider these independent estimates to be essentially in agreement and collectively they suggest the total mass of Hamburg is of the order tens to at most a few hundred kilograms.

A final energy comparison/estimate may be made using the relationship between peak brightness and total energy found among U.S. Government sensor bolides presented by Gi et al. (2018) (their equation 5). Using our GLM and video lightcurve result that the brightest flare for Hamburg had a peak absolute magnitude of −16.3, we find that the Gi et al. (2018) relation predicts an integrated total energy of 7 T TNT equivalent, in excellent agreement with our other estimates.

Considering the lightcurve, ablation modeling, infrasonic energy estimate, and energy/magnitude relation together, our preferred total energy range for the Hamburg fireball is 2–7 T TNT (8.4–28 × 10⁹ J), which corresponds to a preferred mass range of 60–225 kg. We consider the upper end of this range the most probable. This implies that the Hamburg meteoroid had an initial diameter in the range 0.3–0.5 m.
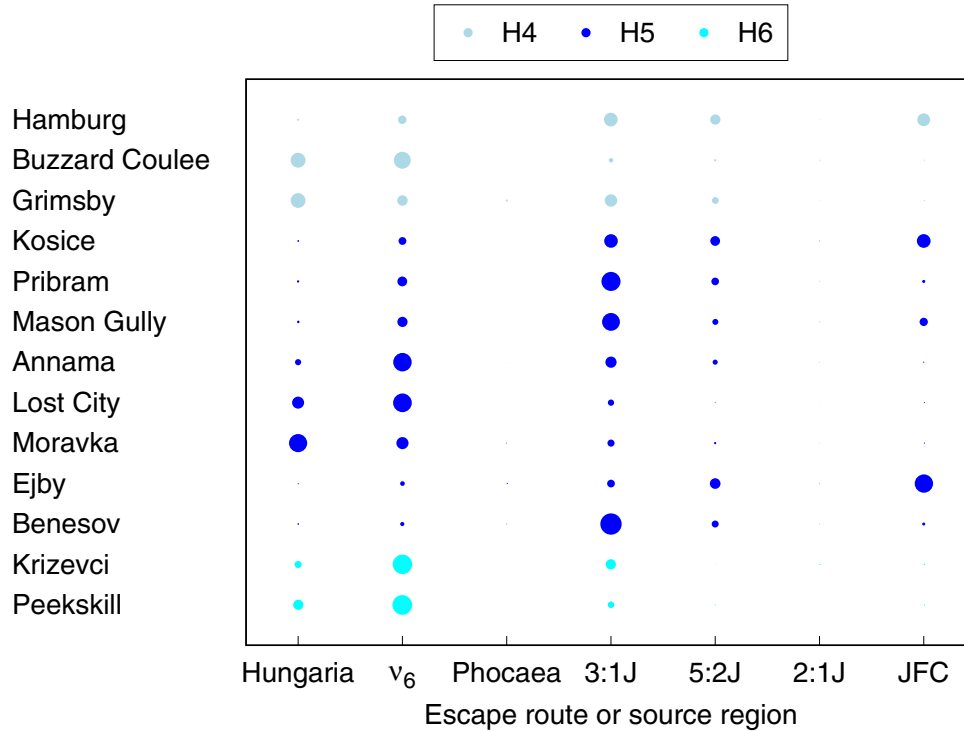
Fig. 15. Escape-route probabilities for known H chondrites including the Hamburg meteorite. The symbol size is proportional to the probability that the measured meteorite orbit at the orbital distance of the Earth, originated from a given escape route in the Main Belt (see Granvik et al. [2016, 2018] for details of the model).

Orbital Evolution History and Comparison to Other H chondrite orbits

In estimating the ER of the Hamburg meteorite from the asteroid belt or an ecliptic cometary source, we follow the approach described in Granvik and Brown (2018), which utilizes the NEO population model by Granvik et al. (2016). Using the semi-major axis, eccentricity, and inclination as reported in Table 3 (and including the Monte Carlo fit uncertainties, which we emphasize are likely lower limits), we find that Hungaria, Phocaea, and the 2:1J MMR complex have negligible ER probabilities (<<1%) whereas the 3:1J MMR complex (36 $\pm$ 8%), Jupiter-family-comet (JFC) region (35 $\pm$ 14%), the 5:2J MMR complex (16 $\pm$ 8%), and the ν_6 secular resonance (12 $\pm$ 3%) have significant probabilities. The most striking feature of these probabilities is that there is not a single ER that would clearly stand out. This is partly due to the fact that the orbit of Hamburg and many other H chondrites fall in the densest region of the NEO steady-state orbit distribution which is fed roughly equally by multiple ERs.

The probability for the 5:2J complex is reduced to about 1% and the JFC probability comparably increased (56 $\pm$ 8%) if one changes the NEO model by

Granvik et al. (2016) to the model by Granvik et al. (2018). Probabilities for the other ERs remain statistically unchanged. The difference between the two NEO models is that the disruption at small perihelion distance (q) was modeled differently—Granvik et al. (2016) excluded test particles that reached a critical q when constructing steady-state orbit distributions whereas Granvik et al. (2018) constructed steady-state orbit distributions without considering the disruption and instead used a penalty function (with fitted parameters) to discard the predicted excess of NEOs with small q. Hence, a small difference in steady-state orbit distributions may explain the difference in ER predictions. This interpretation is also supported by the fact that the probability predictions for JFC and 5:2J complex have the largest error bars when using the Granvik et al. (2016) model and agree on the 2-σ level with 56% for JFC and 1% for the 5:2J complex.

The Hamburg meteorite orbit adds evidence to a mid to outer belt source region for H chondrite although an escape through ν_6 cannot be excluded (Fig. 15). The two previously known H4 chondrites (Buzzard Coulee and Grimsby) are likely to originate in the inner asteroid belt or the Hungaria region, albeit from a higher inclination source; Hamburg is the first low inclination H4 orbit. The Hamburg orbit and,

consequently, ER probabilities are most similar to the Kosice, Ejby, and Mason Gully meteorites, all classified as H5. We note that Hamburg is the fourth H chondrite with a significant probability for an origin in the JFC region, although this may just be a reflection of the overlapping contributions from multiple ERs in this part of the orbital space.

The small orbital inclination of Hamburg would seem to indicate that asteroid (6) Hebe with an inclination of about 15° is unlikely to be the source for H chondrites, particularly as 7 (including Hamburg) of the 14 known H chondrite orbits are under 5° inclination. However, this is not a strong conclusion as a fraction of test particles that start on high-inclination orbits in the asteroid belt may evolve to low-inclination orbits in the near-Earth space (Granvik et al. 2017). Since meteoroids on low-inclination orbits are more likely to impact the Earth compared to those on high-inclination orbits, one would expect the sample of meteoroids and meteorites coming from Hebe to be positively biased toward low inclinations. Thus, while we cannot conclusively identify the source body of H chondrites, the data at hand suggest that a mid to outer belt source region for H chondrites is likely and a parent at low inclination would be favored. Nevertheless, we emphasize that (6) Hebe is located in this region of the asteroid belt and so cannot be ruled out, provided some daughter fragments from Hebe migrate to low inclinations and there is a large enough reservoir of such bodies.

CONCLUSIONS

The Hamburg fireball entered the atmosphere at 15.83 ± 0.05 km s^{-1} at a steep angle (only 24° from the vertical) from a radiant to the ESE of Hamburg Lake, Michigan, resulting in a comparatively compact strewn field oriented almost east–west. Based on darkflight modeling, comparison to meteorite recovery locations and masses together with interpretation of the Doppler radar signature of the falling debris curtain, most recovered fragments originated near the terminal point of the fireball. Some larger fragments may have been separated at the flares to reach darkflight near 20 km altitude, but none of the recovered meteorite masses/locations are consistent with an origin much higher than the first flare. As our entry modeling and the Doppler radar signature suggests a large number of small (<100 g) fragments were produced, the darkflight results predict material in the tens of gram range from the flares would not be primarily found on the lake surfaces, but rather on land between Strawberry Lake and Hamburg Lake where few fragments were recovered. Lack of material from these flares may be due in part to the more difficult search conditions in this region.

The video-derived lightcurve and GLM-derived lightcurve show relative timing and magnitude agreement, though the GLM recorded only the two brightest flares. These flares are centered at heights of 24.1 and 21.7 km, respectively, where the dynamic pressure was 5–7 MPa, suggesting this was the global strength of the bulk of the Hamburg meteoroid. Early minor fragmentation may have occurred near 0.3 MPa, but the evidence for this is not conclusive. That the Hamburg fireball lightcurve derived from video data is consistent supports the claim of Jenniskens et al. (2018) that the GLM sensitivity is near an absolute magnitude of −14.

The Hamburg meteoroid had a preatmospheric diameter between 0.3 and 0.5 m, equivalent to an initial mass in the 60–225 kg range or a total fireball initial kinetic energy of 2–7 T TNT. Objects the size of Hamburg impact Earth daily (Brown et al. 2002). Based on its preatmospheric orbit, the Hamburg H4 chondrite originated in the mid to outer belt. No specific parent body can yet be identified for the H chondrites based on available preatmospheric orbits, but the low inclination of Hamburg together with half of all known H chondrite orbits favors a low inclination parent in the mid to outer belt, though (6) Hebe cannot be strictly ruled out.

to search public lands in support of our scientific study. Finally, we thank Brandon Weller, Ron Matthews, Lisa Matthews, Ashley Moritz, Chris Rodgers, Luke Janes, David Eagen, and others who wish to remain anonymous for sharing the locations and masses of the meteorites that they found. The FM model code was kindly provided by Z. Ceplecha, P. Spurny, and J. Borovička and the MILIG code by J. Borovička. Helpful discussions with W.F. Bottke are gratefully acknowledged. We also thank Professor David Sept of the Center for Computational Medicine and Bioinformatics at the University of Michigan for bringing this fireball to our prompt attention. We thank G. Tancredi and P. Spurny for careful reviews of an earlier version of this manuscript. Very helpful discussions with J. Borovička and P. Spurny related to trajectory measurement uncertainty in particular are gratefully acknowledged.

Editorial Handling—Josep M. Trigo-Rodríguez

REFERENCES

Binzel R. P., Reddy V., and Dunn T. 2015. The near-earth object population: Connections to comets, main-belt asteroids, and meteorites. In *Asteroids IV*, edited by Michel P., DeMeo F. E., and Botke W. F. Tucson, Arizona: University of Arizona Press. pp. 243–256.

Borovička J. 1990. The comparison of two methods of determining meteor trajectories from photographs. *Bulletin of the Astronomical Institutes of Czechoslovakia* 41:391–396.

Borovička J. 2014. *The analysis of casual video records of fireballs*, edited by Gyssens M., Roggemans P., and Zoladek P. Proceedings of the International Meteor Conference, Poznan, Poland, 22–25 August 2013. pp. 101–105.

Borovička J. and Kalenda P. 2003. The Morávka meteorite fall: 4. Meteoroid dynamics and fragmentation in the atmosphere. *Meteoritics & Planetary Science* 38:1023–1043.

Borovička J. and Spurný P. 1996. Radiation study of two very bright terrestrial bolides and an application to the comet S-L 9 collision with Jupiter. *Icarus* 121:484–510.

Borovička J., Tóth J., and Igaz A. 2013a. The Košice meteorite fall: Atmospheric trajectory, fragmentation, and orbit. *Meteoritics & Planetary Science* 48:1757–1779.

Borovička J., Spurný P., Brown P. G., Wiegert P. A., Kalenda P., Clark D., and Shrbený L. 2013b. The trajectory, structure and origin of the Chelyabinsk asteroidal impactor. *Nature* 503:235–237.

Borovička J., Spurný P., and Brown P. G. 2015. Small near-earth asteroids as a source of meteorites. In *Asteroids IV*, 4th ed. Arizona, Tucson: University of Arizona Press. pp. 257–280.

Brown P. G., Spalding R. E., ReVelle D. O., Tagliaferri E., and Worden S. P. 2002. The flux of small near-Earth objects colliding with the Earth. *Nature* 420:294–296.

Brown P., Weryk R. J., Kohut S., Edwards W. N., and Krzeminski Z. 2010. Development of an all sky video Meteor Network in Southern Ontario, Canada: The ASGARD system. *Journal of the International Meteor Organization* 38:18–23.

Brown P. G., McCausland P. J. A., Fries M., Silber E., Edwards W. N., Wong D. K., Weryk R. J., Fries J., and Krzeminski Z. 2011. The fall of the Grimsby meteorite-I: Fireball dynamics and orbit from radar, video, and infrasound records. *Meteoritics & Planetary Science* 363:339–363.

Brown P. G., Assink J. D., Astiz L., Blaauw R., Boslough M. B., Borovička J., Brachet N., Brown D., Campbell-Brown M., Ceranna L., Cooke W., de Groot-Hedlin C., Drob D. P., Edwards W., Evers L. G., Garces M., Gill J., Hedlin M., Kingery A., Laske G., Le Pichon A., Mialle P., Moser D. E., Saffer A., Silber E., Smets P., Spalding R. E., Spurn P. Ý, Tagliaferri E., Uren D., Weryk R. J., Whitaker R., and Krzeminski Z. 2013. A 500-kiloton airburst over Chelyabinsk and an enhanced hazard from small impactors. *Nature* 503: 238–241.

Ceplecha Z. 1987. Geometric, dynamic, orbital and photometric data on meteoroids from photographic fireball networks. *Astronomical Institutes of Czechoslovakia, Bulletin* 38:222–234.

Ceplecha Z. and ReVelle D. O. 2005. Fragmentation model of meteoroid motion, mass loss, and radiation in the atmosphere. *Meteoritics & Planetary Science* 40:35–54.

Ceplecha Z., Borovička J., Elford W., ReVelle D., Hawkes R. L., Poruban V., and Simek M. 1998. Meteor phenomena and bodies. *Space Science Reviews* 84:327–471.

Christian H. J., Blakeslee R. J., Goodman S. J., Mach D. A., Stewart M. F., Buechler D. E., Koshak W. J., Hall J. M., Boeck W. L., Driscoll K. T., and Boccippio D. J. 1999. *The Lightning Imaging Sensor*. 11th Int. Conf. on Atmospheric Electricity. Guntersville, AL: ICAE. pp. 746–749.

Cooke W. J. and Moser D. E. 2012. The status of the NASA all sky fireball network. *Proceedings of the International Meteor Conference* 2011:9–12.

Crum T. and Alberty R. 1993. The WSR-88D and the WSR-88D operational support facility. *Bulletin of the American Meteorological Society* 74:1669–1687.

Devillepoix H. A. R., Sansom E. K., Bland P. A., Towner M. C., Cupák M., Howie R. M., Jansen-Sturgeon T., Cox M. A., Hartig B. A. D., Benedix G. K., and Paxman J. P. 2018. The Dingle Dell meteorite: A Halloween treat from the Main Belt. http://arxiv.org/abs/1803.02557.

Ens T. A., Brown P. G., Edwards W. N., and Silber E. 2012. Infrasound production by bolides: A global statistical study. *Journal of Atmospheric and Solar-Terrestrial Physics* 80:208–229.

Fieber-Beyer S. K. and Gaffey M. J. 2014. Near-infrared spectroscopy of 3:1 Kirkwood Gap asteroids II: Probable and plausible parent bodies: Primitive and differentiated. *Icarus* 229:99–108.

Folinsbee R. E. and Bayrock L. A. 1961. The Bruderheim meteorite—Fall and recovery. *Journal of the Royal Astronomical Society of Canada* 55:218–228.

Fries M. 2018. Using weather imagery to find meteorite falls, presentation at the All Sky Meteor Network workshop, held at NASA Ames, March 13, 2018.

Fries M. and Fries J. 2010. Doppler weather radar as a meteorite recovery tool. *Meteoritics & Planetary Science* 45:1476–1487.

Gaffey M. J. and Gilbert S. L. 1998. Asteroid (6) Hebe: the probable parent body of the H-type ordinary chondrites and the IIE iron meteorites. *Meteoritics & Planetary Science* 1295:1281–1295.

Gi N., Brown P., and Aftosmis M. J. 2018. The frequency of window damage caused by bolide airbursts: A quarter century case study. *Meteoritics & Planetary Science* 53:1413–1431.

Goodman S. J., Blakeslee R. J., Koshak W. J., Mach D. M., Bailey J. C., Buechler D. E., Carey L. D., Schultz C. D., Bateman M., McCaul E. W., and Stano G. 2013. The GOES-R geostationary lightning mapper (GLM). *Atmospheric Research* 125–126:34–49.

Granvik M. and Brown P. 2018. Identification of meteorite source regions in the solar system. *Icarus* 311:271–287.

Granvik M., Morbidelli A., Jedicke R., Bolin B., Bottke W. F., Beshore E., Vokrouhlicky D., Delbo M., and Michel P. 2016. Super-catastrophic disruption of asteroids at small perihelion distances. *Nature* 530:303–306.

Granvik M., Morbidelli A., Vokrouhlicky D., Bottke W. F., Nesvorny D., and Jedicke R. 2017. Escape of asteroids from the main belt. *Astronomy & Astrophysics* 598:A52.

Granvik M., Morbidelli A., Jedicke R., Bolin B., Bottke W. F., Beshore E., Vokrouhlicky D., Nesvorny D., and Michel P. 2018. Debiased orbit and absolute-magnitude distributions for near-Earth objects. *Icarus* 312:181–207.

Halliday I., Blackwell A. T., and Griffin A. A. 1984. The frequency of meteorite falls on the earth. *Science* 223:1405–1407.

Heck P. and Greer J. 2018. Meteoritical Bulletin no. 107.

Hedlin M. A. H., Ritsema J., de Groot-Hedlin C. D., and Hetland E. A. 2018. A multidisciplinary study of the 17 January 2018 bolide terminal burst over Southeast Michigan. *Seismological Research Letters* 89:2183–2192.

Jenniskens P., Albers J., Tillier C. E., Edgington S. F., Longenbaugh R. S., Goodman S. J., Rudlosky S. D., Hildebrand A. R., Hanton L., Ciceri F., Nowell R., Lyytinen E., Hladiuk D., Free D., Moskovitz N., Bright L., Johnston C. O., and Stern E. 2018. Detection of meteoroid impacts by the Geostationary Lightning Mapper on the GOES-16 satellite. *Meteoritics & Planetary Science* 25:1–25.

Mach D., Christian H., Blakeslee R., Boccippio D., Goodman S., and Boeck W. 2007. Performance assessment of the optical transient detector and lightning imaging sensor. Part II: clustering algorithm. *Journal of Geophysical Research* 112:D09210.

Marsset M., Carry B., Dumas C., Hanuš J., Viikinkoski M., Vernazza P., Müller T. G., Delbo M., Jehin E., Gillon M., Grice J., Yang B., Fusco T., Berthier J., Sonnett S., Kugel F., Caron J., and Behrend F. 2017. 3D shape of asteroid (6) Hebe from VLT/SPHERE imaging: Implications for the origin of ordinary H chondrites. *Astronomy & Astrophysics* 604:A64.

Perlerin V. 2018. https://www.amsmeteors.org/2018/01/bright-fireball-spotted-over-michigan/

Popova O. P., Borovička J., Hartmann W. K., Spurný P., Gnos E., Nemtchinov I. V., and Trigo-Rodriguez J. M. 2011. Very low strengths of interplanetary meteoroids and small asteroids. *Meteoritics & Planetary Science* 46:1525–1550.

ReVelle D. O. and Ceplecha Z. 2001. Bolide physical theory with application to PN and EN fireballs. In *Proceedings of the Meteoroids 2001 Conference, 6–10 August 2001, Kiruna, Sweden*, edited by Warmbein B. Noordwijk, the Netherlands: ESA Publications Division. pp. 507–512.

Silber E. and Brown P. G. 2014. Optical observations of meteors generating infrasound—I: Acoustic signal identification and phenomenology. *Journal of Atmospheric and Solar-Terrestrial Physics* 119:116–128.

Spurný P., Borovička J., Kac J., Kalenda P., Atanackov J., Kladnik G., Heinlein D., and Grau T. 2010. Analysis of instrumental observations of the Jesenice meteorite fall on April 9, 2009. *Meteoritics & Planetary Science* 45:1392–1407.

Tóth J., Svore J., Borovička P., Spurn A., Igaz L., Korno P., Vereš M., Husárik J., Koza A., Kučera P., Zigo Š., Gajdoš J., Világi D., Čapek Z., Krišandová D., Tomko J., Šilha J., Schunová E., Bodnárová M., Búzová D., and Krejčová T. 2015. The Košice meteorite fall: Recovery and strewn field. *Meteoritics & Planetary Science* 50:853–863.

Vernazza P., Zanda B., Binzel R. P., Hiroi T., DeMeo F. E., Birlan M., Hewins R., Ricci L., Barge P., and Lockhart M. 2014. Multiple and fast: the accretion of ordinary chondrite parent bodies. *Astrophysical Journal* 791:120

Vida D., Brown P. G., and Campbell-Brown M. 2018. Modelling the measurement accuracy of pre-atmosphere velocities of meteoroids. *Monthly Notices of the Royal Astronomical Society* 479:4307–4319.

Vida D., Gural P. S., Brown P. G, Campbell-Brown M., and Wiegert P. 2019. Estimating trajectories of meteors: An observational Monte Carlo Approach, in revision, Monthly Notices of the Royal Astronomical Society.

Vokrouhlický D. and Farinella P. 2000. Efficient delivery of meteorites to the Earth from a wide range of asteroid parent bodies. *Nature* 407:606–608.

Weryk R. J. and Brown P. G. 2012. Simultaneous radar and video meteors—I: metric comparisons. *Planetary and Space Science* 62:132–152.

SUPPORTING INFORMATION

Additional supporting information may be found in the online version of this article.

Appendix S1. Calibration details and trajectory solution for the Hamburg fireball.